

1 **Title:** A mechanistic erosion model for cosmogenic nuclide inheritance in fluvial  
2 single-clast exposure ages

3  
4  
5  
6  
7  
8  
9 Veronica B. Prush<sup>a,\*</sup>, Michael E. Oskin<sup>a</sup>

10  
11 <sup>a</sup>Department of Earth and Planetary Sciences  
12 University of California, Davis  
13 1 Shields Avenue  
14 Davis, CA 95616  
15 United States

16  
17 \*Corresponding Author  
18

19 Prush Contact Information:  
20 vbprush@ucdavis.edu

21  
22 Oskin Contact Information:  
23 meoskin@ucdavis.edu  
24

25  
26  
27 *This is a non-peer reviewed preprint submitted to EarthArXiv. This article is*  
28 *currently (08/2019) submitted to Earth and Planetary Science Letters.*  
29

30 **Abstract**

31 Terrestrial cosmogenic nuclides (TCNs), produced by the bombardment of Earth's  
32 surface by cosmic rays, are widely used for age-dating and pacing surface processes. Sediments  
33 carry an inherited TCN concentration, useful for quantifying erosion and transport rates, but that  
34 must be subtracted when age-dating sedimentary landforms, such as alluvial fans. Here we  
35 present a mechanistic model of inheritance based on the contributions of episodic erosion by  
36 landsliding and steady, background erosion due to soil formation. The balance of these  
37 processes, revealed by the distribution of inheritance recorded by a population of individual  
38 surface clasts, affects rates of soil generation and the cycling of material through the Earth's  
39 critical zone – the surficial layer upon which all terrestrial life depends. We test our inheritance  
40 model on alluvial fan TCN datasets drawn from a global compilation of active-fault slip-rate  
41 studies. Inheritance-corrected landform ages are systematically younger than published ages. Our  
42 results reveal a consistent signature of spatiotemporal clustering of landslides, important for  
43 quantifying hazard and for understanding the coupling of physical and chemical erosion.  
44 Application of our inheritance model provides a rigorous approach to correcting landform ages  
45 for inheritance and reveals information on landslide frequency, with broad implications for  
46 hazard and land use.

47 **Keywords:** Cosmogenic radionuclides, Erosion, Landslides, generalized Pareto distribution

48

49 **1. Introduction:**

50 Terrestrial cosmogenic nuclide (TCN) techniques have revolutionized the field of  
51 geomorphology by providing a means for constraining landform ages and rates of surface  
52 processes over the Quaternary (e.g., Gosse and Phillips, 2001; Lal, 1991). This time period is key

53 to quantifying natural hazard recurrence and modeling land-surface processes relevant to society.  
54 Such processes include earthquake hazard models and forecasts, which are underpinned by  
55 estimates of fault motion based on age-dating of offset Quaternary deposits (e.g., Page et al.,  
56 2014), and calculation of erosion rates, which quantify the stripping and regeneration rates of soil  
57 (e.g., Granger and Riebe, 2013).

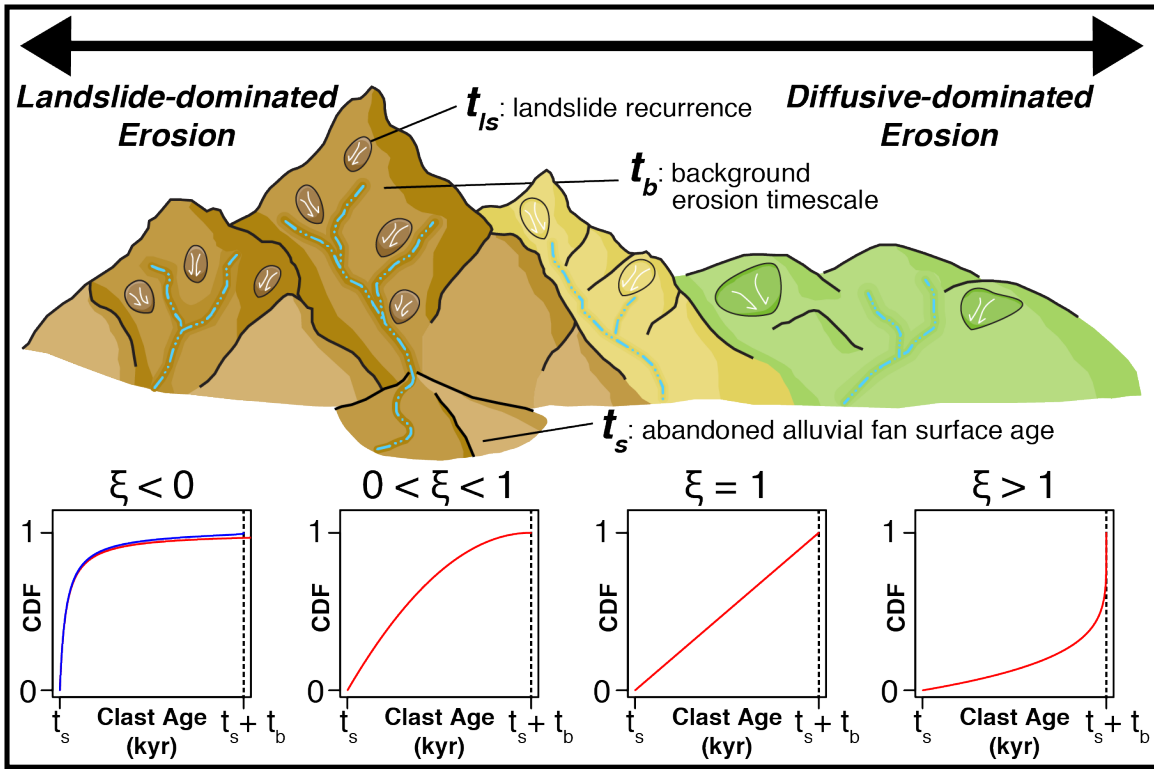
58 TCNs are produced during the bombardment of Earth's surface by cosmic rays. Cosmic  
59 rays enter the atmosphere and produce new nuclides by spallation (Cerling and Craig, 1994;  
60 Gosse and Phillips, 2001; Lal, 1991). The production rate of TCNs is a function of shielding (for  
61 example, by topographic blocking), elevation, atmospheric pressure, and geomagnetic field  
62 intensity (Cerling and Craig, 1994; Gosse and Phillips, 2001; Lal, 1991; Lifton et al., 2014;  
63 Stone, 2000). Isotopes commonly used in geomorphological applications include Beryllium-10,  
64 Aluminum-26, Chlorine-36, Helium-3, and Neon-21. Because TCN production occurs mostly in  
65 the upper two meters of Earth's surface (Lal, 1991), TCN concentrations are widely used to track  
66 sediment erosion and transport. For surface age-dating applications, TCN concentration acquired  
67 during erosion constitutes an added age component, referred to as inheritance, that must be  
68 removed (e.g., Anderson et al., 1996).

69 In eroding landscapes lacking long-term sediment storage, the mean concentration of the  
70 TCN Beryllium-10 ( $^{10}\text{Be}$ ) in quartz from well-mixed river sand may be interpreted as a steady  
71 erosion rate of the source catchment (Brown et al., 1995; Niemi et al., 2005). However, this  
72 model does not account for the episodic nature of erosion processes, in particular by landsliding,  
73 shown numerically to strongly bias TCN erosion rate measurements (e.g., Niemi et al., 2005;  
74 West et al., 2014; Yanites et al., 2009). Landslides dominate erosion of actively uplifting  
75 mountain ranges (Korup et al., 2010). Decadal studies show that extreme events, such as major

76 storms and earthquakes, modulate landslide occurrence (Dadson et al., 2003; McPhillips et al.,  
77 2014; West et al., 2014), temporarily increasing sediment yield and solute flux (Emberson et al.,  
78 2016; West et al., 2014). Simulations of landslide recurrence predict a patchwork renewal of  
79 landscapes (Niemi et al., 2005; Yanites et al., 2009), episodically exposing fresh rock surfaces to  
80 weathering. Because chemical weathering and soil production rates decline over time as regolith  
81 forms (Gabet, 2007; Taylor and Blum, 1995), the feedback between physical and chemical  
82 erosion, critical to understanding coupling of erosion to atmospheric carbon dioxide and organic  
83 carbon cycling (Kump et al., 2000), depends on landslide renewal time and its spatial variation.  
84 In addition to geomorphic and landscape evolution consequences, quantifying the long-term,  
85 catchment-wide recurrence behavior of landslides is essential for mitigating their environmental  
86 and hazard consequences.

87         Here we derive a mechanistic model for the distribution of terrestrial cosmogenic nuclide  
88 (TCN) exposure ages within a population of sedimentary clasts, based on balance of landslide  
89 frequency and steady, background erosion in the source catchment (Fig. 1). To test the  
90 applicability of this model, we analyze 64 clast-age datasets drawn from the literature (Table S1),  
91 primarily fault slip-rate studies with exposure age dating applied to alluvial fans and stream  
92 terraces. From a population of surface clast  $^{10}\text{Be}$  measurements (boulder or cobble), these studies  
93 commonly estimate surface age from the mean of the youngest cluster of clast ages, which are  
94 assumed to lack inheritance (e.g., Van Der Woerd et al., 2002). However, such clustering is not  
95 always apparent, and the filtering and averaging employed assumes clast ages should be  
96 normally distributed. We show that inheritance resulting from a combination of steady,  
97 background erosion and episodic landslides follows a generalized Pareto distribution. This  
98 probabilistic model of clast inheritance permits rigorous assessment of its contribution to sample

99 ages, and generally results in younger landform dates than published. This model also explains  
 100 the spectrum of observed clast-age distributions, attributable to catchment-scale variations in  
 101 landslide recurrence and erosion rates.  
 102



103  
 104 **Fig. 1.** Schematic catchment model of landslide erosion's influence on clast-age distribution.  
 105 Red lines show clast-age distributions modeled as generalized Pareto cumulative distribution  
 106 functions (CDFs). Decreasing values of the shape parameter,  $\xi$ , are indicative of catchments  
 107 where erosion by landslides contributes proportionally more sediment to drainages than erosion  
 108 by soil formation and diffusive down-slope transport. For positive values,  $\xi$  may be interpreted  
 109 as  $t_{ls}/t_b$ , the ratio of average landslide recurrence, derived with a Poisson landslide recurrence  
 110 model, to background erosion timescale, defined as the time required to erode through one e-  
 111 folding length scale ( $\sim 60$  cm in rock; Lal, 1991). Negative  $\xi$  values require long-tailed, non-

112 Poisson landslide recurrence. Blue line shows an equivalent CDF derived with Pareto-distributed  
113 (long-tailed) landslide return times (see Section 2.1).

114

## 115 **2. Model Derivation and Distribution-fitting Approach**

### 116 **2.1 Clast-age model derivation**

117 Following the approach of previous studies (Niemi et al., 2005; Yanites et al., 2009), we  
118 model catchment erosion as a combination of landslides, which episodically erode and reset the  
119 nuclide concentration in catchment walls, and diffusive background erosion processes, which  
120 steadily erode the surface between landslide events. Our analytical approach does not directly  
121 account for the volume of landslides. Rather, we derive the TCN concentration in clasts eroded  
122 from the catchment wall following the most recent landslide event. This has been shown to  
123 compare well with numerical simulations that explicitly account for landslide volume (e.g.,  
124 Yanites et al., 2009).

125 Between landslide events, the catchment wall undergoes a steady, background regolith  
126 erosion rate,  $E_b$ , during which TCNs accumulate according to an exponential ingrowth curve  
127 approaching a maximum steady-state effective exposure age,  $t_b = z^*/E_b$ , where  $z^*$  is the e-  
128 folding length of TCN production by nuclide spallation (~60 cm for a typical bedrock density of  
129  $2.7 \text{ g/cm}^3$ , Fig. 1)(e.g., Lal, 1991). We refer to  $t_b$  herein as the background erosion timescale.  
130 Background erosion is an aggregate term that refers to any diffusive erosional process, such as  
131 soil creep. Starting with zero TCN concentration, the effective TCN age of the catchment wall,  
132 and thus the effective age of sediment clasts derived from that portion of the landscape ( $t_c$ ),  
133 exponentially approaches  $t_b$ :

$$134 \quad t_c = t_b(1 - e^{-t/t_b}) \quad (1)$$

135 In accordance with previous studies (Niemi et al., 2005; Yanites et al., 2009), we initially  
136 choose to model landslide recurrence as a Poisson process with a wait time probability  
137 distribution function (PDF):

$$138 \quad PDF(wt) = \frac{1}{t_{ls}} e^{-t/t_{ls}} \quad (2)$$

139 where  $t_{ls}$  is the mean wait time between landslides at every point within a catchment. A Poisson  
140 model implies that wait times between landslides are spatiotemporally uncorrelated (e.g.,  
141 Crovelli, 2000; Witt et al., 2010; Yanites et al., 2009).

142 Combining landslide recurrence and TCN ingrowth yields a probabilistic model for the  
143 past exposure history of a landscape from which a sediment sample is derived. We determine the  
144 probability distribution function (PDF) of clast ages due to TCN ingrowth and landslide renewal  
145 by substituting the relation for background erosion ( $t_c$ , Eq. 1) into the Poisson PDF of landslide  
146 recurrence and multiply by the Jacobian derivative ( $dt/dt_c$ ) to maintain probability (Yanites et  
147 al., 2009):

$$148 \quad PDF(t_c) = PDF(wt, t = f(t_c)) dt/dt_c \quad (3)$$

149 where  $t = -t_b \ln(1 - t_c/t_b)$  and  $\frac{dt}{dt_c} = \frac{1}{1 - \frac{t_c}{t_b}}$ . The result is a generalized Pareto distribution  
150 (GPD) of clast ages,  $t_c$ :

$$151 \quad PDF(t_c) = \frac{1}{t_{ls}} \left[ 1 - \frac{t_c}{t_b} \right]^{t_b/t_{ls} - 1} \quad (4)$$

152 The cumulative distribution function (CDF) associated with this PDF is found by  
153 integrating Eq. 4 from 0 to  $t_c$ , and allowing for a shift,  $t_s$ , due to post-depositional aging of the  
154 deposit (the target surface age of datasets used in this study):

155 
$$CDF_{GPD}(t_c) = 1 - \left[ 1 - \frac{(t_c - t_s)}{t_b} \right]^{t_b/t_{ls}} \quad (5)$$

156 This CDF is the three-parameter form of the GPD. The three parameters of the GPD are known  
157 as location, shape, and scale, which taken together describe its general form. Location defines the  
158 intercept of a dataset's GPD distribution (where  $CDF_{GPD} = 0$ ), shape defines its concavity, and  
159 scale defines its curvature. Under the conditions of Poisson landslide recurrence,  $t_s$ ,  $\xi = t_{ls}/t_b$ ,  
160 and  $\sigma = t_{ls}$  are the location, shape, and scale parameters of the GPD distribution, respectively.  
161 These parameters reveal the post-depositional age of the surface from which the sample was  
162 collected ( $t_s$ ), and two timescales related to erosion of the source catchment: average landslide  
163 recurrence ( $t_{ls}$ ), and background erosion timescale ( $t_b$ ).

164 Long-tailed GPD distributions of clast ages, described by  $\xi < 0$ , cannot be explained by  
165 Poissonion landslide recurrence, because neither  $t_b$  nor  $t_{ls}$  may be negative. Instead, the  
166 underlying landslide wait time model must also be a long-tailed. To explore this, we recast our  
167 derivation using a member of the Pareto distribution family, the Lomax distribution (Lomax,  
168 1954), for the landslide wait time:

169 
$$PDF_{LO}(wt) = \frac{\alpha}{\beta} \left[ 1 + \frac{t}{\beta} \right]^{-(\alpha+1)} \quad (6)$$

170 The parameters  $\alpha$  and  $\beta$  are the tail and scale parameters, respectively, of this distribution. The  
171 mean landslide return time is  $\beta/(\alpha - 1)$ . Note that these parameters are distinct from the shape  
172 and scale parameters defined by eq. 5, though they are related, as shown below.

173 The derivation for  $PDF_{LO}(t_c)$  follows the same steps as above for the Poisson case (eqs.  
174 1-5). For clarity, we omit shifting the distribution by a location value,  $t_s$ . The resulting PDF and  
175 CDF are:



176 
$$PDF_{LO}(t_c) = \frac{\alpha}{\beta} \left[ 1 - \frac{t_b}{\beta} \ln \left( 1 - \frac{t_c}{t_b} \right) \right]^{-(\alpha+1)} \frac{-t_b}{1 - \frac{t_c}{t_b}} \quad (7)$$

177 
$$CDF_{LO}(t_c) = 1 - \left[ 1 - \frac{t_b}{\beta} \ln \left( 1 - \frac{t_c}{t_b} \right) \right]^{-\alpha} \quad (8)$$

178  $CDF_{LO}(t_c)$  is closely related to eq. 5. In the limit where  $t_b \gg 0$ , the natural logarithm term may  
179 be approximated with the first term of its Taylor series:

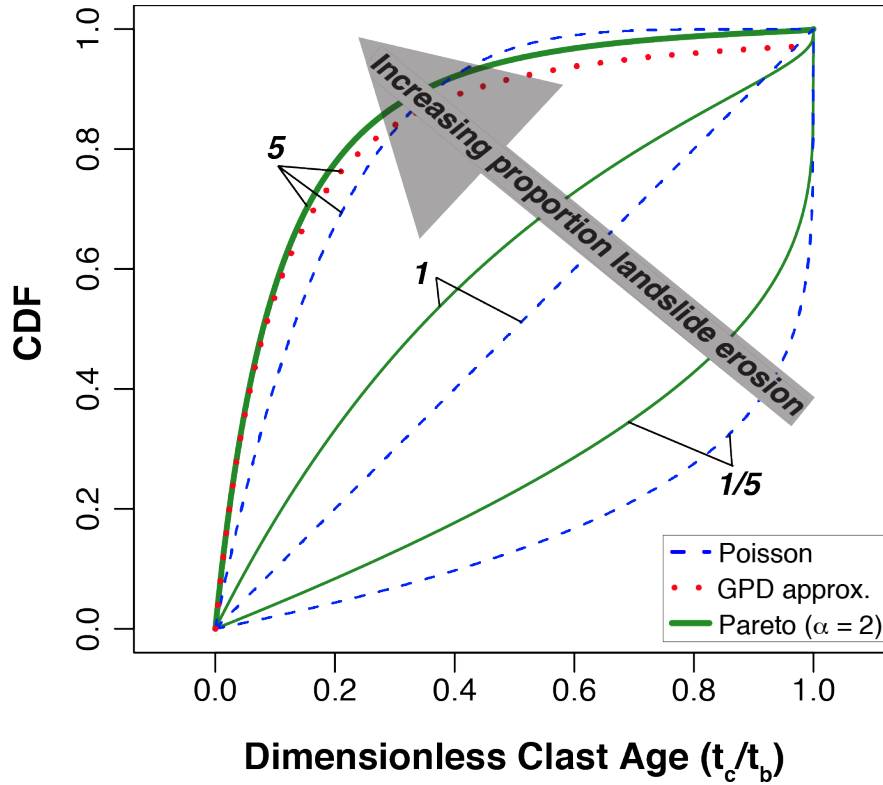
180 
$$\ln \left[ 1 - \frac{t_c}{t_b} \right] \approx -\frac{t_c}{t_b} \quad (9)$$

181 Substitution into  $CDF_{LO}(t_c)$  yields:

182 
$$CDF_{LO}(t_c) \approx 1 - \left[ 1 + \frac{t_c}{\beta} \right]^{-\alpha} \quad (10)$$

183 This CDF is a GPD, analogous to eq. 5, but with  $\xi = -1/\alpha$  as its shape, and  $\sigma = \beta/\alpha$  as its  
184 scale parameter. Therefore, as background erosion rate approaches zero ( $t_b \gg 0$ ), the  
185 distribution of clast ages reflects the distribution of landslide recurrence (eq. 6).

186 Depending on the ratio  $t_b/\beta$  in eq. 8, it may be difficult to discriminate Poisson- and  
187 Pareto-distributed landslide recurrence with limited dataset sizes and TCN measurement  
188 uncertainty (Fig. 2). Fortunately, prediction of the location parameter,  $t_s$ , is insensitive to the  
189 choice of landslide wait-time distribution. However, there are trade-offs between the other  
190 distribution parameters that do depend on this choice. We rely on the GPD clast-age distribution  
191 (eq. 5) to model available datasets, including approximation of long-tailed cases, and defer  
192 application of the full Pareto-distributed landslide model (eq. 8) for future study, as fitting this  
193 model requires larger exposure-age data sets than are currently available.



194

195 **Fig. 2.** Predicted cumulative distribution functions of clast ages derived with Poisson (blue  
 196 dashes) and Pareto (thick, solid green) models of landslide wait time. Clast ages are normalized  
 197 by background erosion time scale,  $t_b$ . Labels indicate mean landslide return time,  $t_{ls}$ , normalized  
 198 by  $t_b$  for each curve ( $\xi$  for Poisson-derived distributions,  $\beta/t_b(\alpha - 1)$  for Pareto-derived  
 199 distributions). These distributions are similar in form when  $t_{ls} \gg t_b$ . Dotted red line shows GPD  
 200 approximation for  $\alpha = 2$  ( $\xi = -1/2$ ) case with  $t_{ls}/t_b = 5$ . This approximation diverges from  
 201 the analogous Pareto-derived clast-age model in the distribution tail, at  $CDF > 0.75$ .

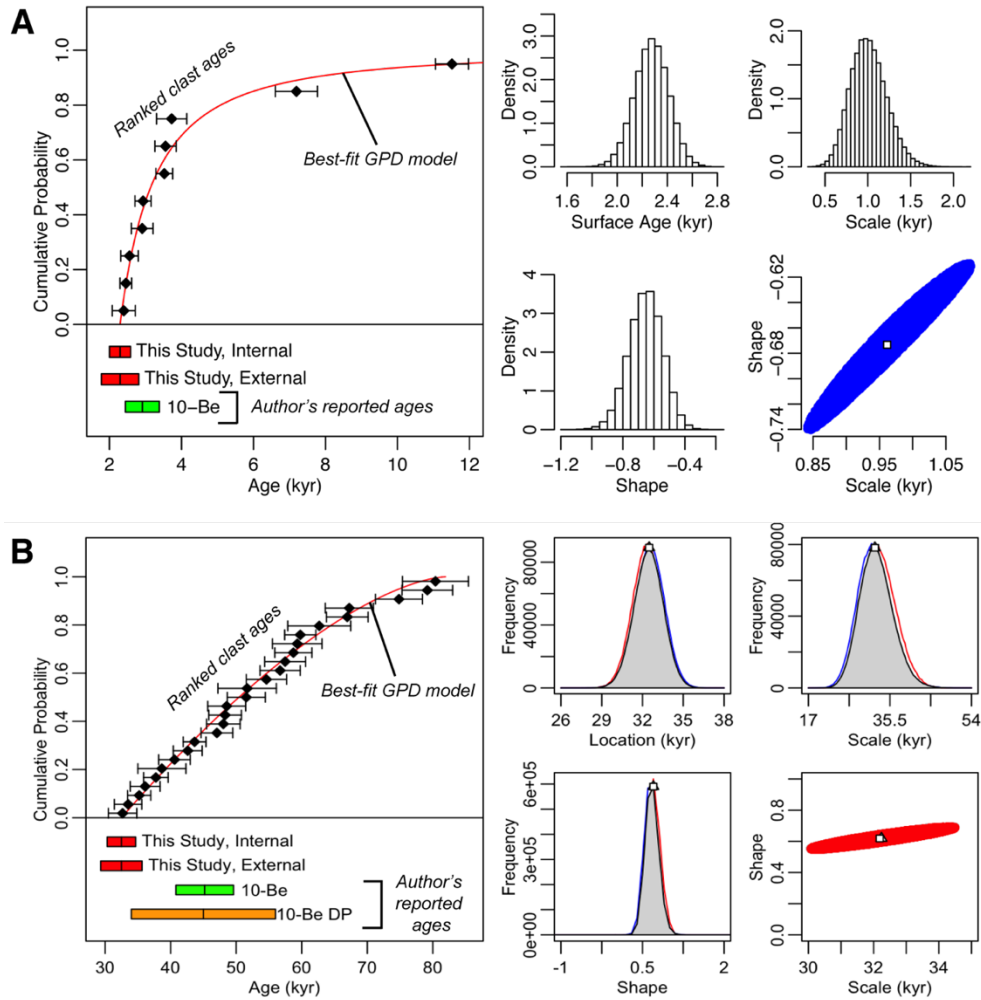
202

203 Several processes that affect TCN concentration in sediments are not included in our  
 204 models. We neglect TCN radioactive decay, an appropriate assumption given the long half-life  
 205 of  $^{10}\text{Be}$  (1.3 Myr) with respect to erosion rates and sediment residence times in the landscape  
 206 (e.g., Granger, 2006; Lal, 1991). We also neglect TCN concentrations acquired during transport

207 following erosion from the catchment walls and prior to deposition within an alluvial fan or  
208 stream terrace, nor do we account for complicated burial histories or reworking of clasts from  
209 upstream deposits. These assumptions are appropriate for short transport distances and  
210 catchments with little sediment storage (Yanites et al., 2009), consistent with the settings of  
211 clast-age datasets we analyze. We assume that the surface TCN concentration will be reset after  
212 each landslide. However, this assumption is not valid for small ( $<100 \text{ m}^2$ ) shallow landslides that  
213 excavate only partway through the upper  $\sim 2 \text{ m}$  (the approximate depth for 95% of TCN  
214 production by spallation)(Lal, 1991). Effectively, the smallest landslides contribute to  
215 background erosion, rather than resetting the TCN concentration of their footprint.

## 216 **2.2 Fitting the model to clast-age distributions**

217 We apply a Bayesian Markov chain Monte Carlo (MCMC) algorithm to sample the  
218 posterior distributions of the three parameters of our GPD model for each data set (Fig. 3). In  
219 multivariate analyses, MCMC algorithms are used to determine the summary statistics of sample  
220 populations where analytical solutions are hampered by model complexity (e.g. Andrieu et al.,  
221 2003). We fit the cumulative GPD to clast ages arranged in rank order, which implicitly assumes  
222 that the underlying distribution was sampled sufficiently and uniformly.



223

224 **Fig. 3.** Annotated example outputs of MCMC algorithm to determine best-fit GPD model to clast

225 age datasets. A) output for  $\xi$ -parameterized algorithm, B) output for combination of  $\theta$  and  $\xi$

226 parameterizations. Diamonds and error bars (two standard deviations, analytical uncertainty

227 only) indicate individual ranked clast ages. Best-fit GPD model indicated by red line. Below x-

228 axis are output ages determined in this study (red bars, 95% range of best-fit solutions) including

229 ages calculated using analytical error only, as well as external error due to TCN production rate

230 uncertainty. If reported, ages determined by publishing authors using  $^{10}\text{Be}$  clasts and other

231 geochronometers are included. DP = depth profile. Right side of each figure shows histograms of

232 accepted output parameters of location ( $t_s$ ), scale ( $\sigma$ ), and shape ( $\xi$ ). Covariance of  $\sigma$  and

233  $\xi$  indicated by bottom right figure, showing best-fit (white box) and field (red or blue) of best 5%  
234 of MCMC-derived parameter fits. Red and blue lines in B indicate results of  $\xi$  and  $\theta$  algorithms  
235 (see text); gray fields are merged probability distributions for each model parameter.

236

237 We determine an initial fit of  $\xi$  and  $\sigma$  using the method of moments (Hosking and Wallis,  
238 1987) and a linear combination of order statistics to determine the best-fit  $t_s$  value (Sazlvadori,  
239 2002). For each parameter, we set the search space (the Bayesian initial prior distribution) to be a  
240 wide normal distribution centered on the initial fit. The step size sample space for each iteration  
241 of the MCMC algorithm is also a normal distribution with a standard deviation that is 5% of the  
242 standard deviation for the initial prior for each parameter. Culling of parameter values is  
243 achieved using log-likelihood minimization with a rejection criterion to eliminate poor  
244 distribution fits. Standard deviation values for the initial prior distribution and step size are  
245 varied together to achieve a 20 to 30% acceptance range, which we consider a satisfactory search  
246 of the available parameter space. We improve on these initial GPD fits over 2 million  
247 realizations of our MCMC algorithm. Acceptable parameter values for the GPD tend to be  
248 normally distributed about the best-fit values (Fig. 3).

249 The range of the shape parameter,  $\xi$ , of the GPD distribution includes two limiting cases.  
250 When  $\xi = 0$ , the GPD simplifies to an exponential distribution, and when  $\xi = 1$  the GPD  
251 behaves as a uniform distribution (e.g., de Zea Bermudez and Kotz, 2010; Hosking and Wallis,  
252 1987). Our algorithm is largely capable of sampling around the limiting case of  $\xi = 0$  without  
253 attrition in the search space of  $\xi$ . However, as  $\xi$  approaches and exceeds 1, the change in  
254 behavior of the GPD (as evidenced by a flip in its concavity, Figs. 1 and 2) requires a different  
255 algorithmic approach. This behavior has been noted previously (de Zea Bermudez and Kotz,

256 2010). In order to sample values of shape near 1 ( $t_{ls} \approx t_b$  for Poisson landslide recurrence), we  
257 introduce an alternative parameterization of the GPD by the exponent  $\theta = \sigma/\xi$ :

$$258 \quad CDF_{GPD}(t_c) = 1 - \left[ 1 - \frac{(t_c - t_s)}{\theta} \right]^{\theta/\sigma}. \quad (11)$$

259

260 In this parameterization, we restrict the search range of  $\theta$  to 0 – 650 kyr.

261

262 The best-fit GPD for most datasets can be determined using one of these two  
263 representations. However, for datasets with a  $\xi$  between 0.5 and 1.5, the search spaces and  
264 resulting best-fit distribution of shape values are truncated near the limiting value of 1. In these  
265 cases, the MCMC outputs from the  $\theta$  and  $\xi$  parameterizations are combined to represent the  
266 summary statistics of the best-fit GPD (Fig. 3b). Distributions for all three GPD parameters are  
267 determined using both algorithms and merged using a linearly tapered weighting scheme for  
268 shape values between 0 and 1. The corresponding  $t_s$  and  $t_{ls}$  parameters are also weighted  
269 according to this scheme. Summary statistics and best-fits of the combined model runs are then  
270 recalculated from the resulting histograms of the model parameters.

### 270 **3. Application of clast-age model**

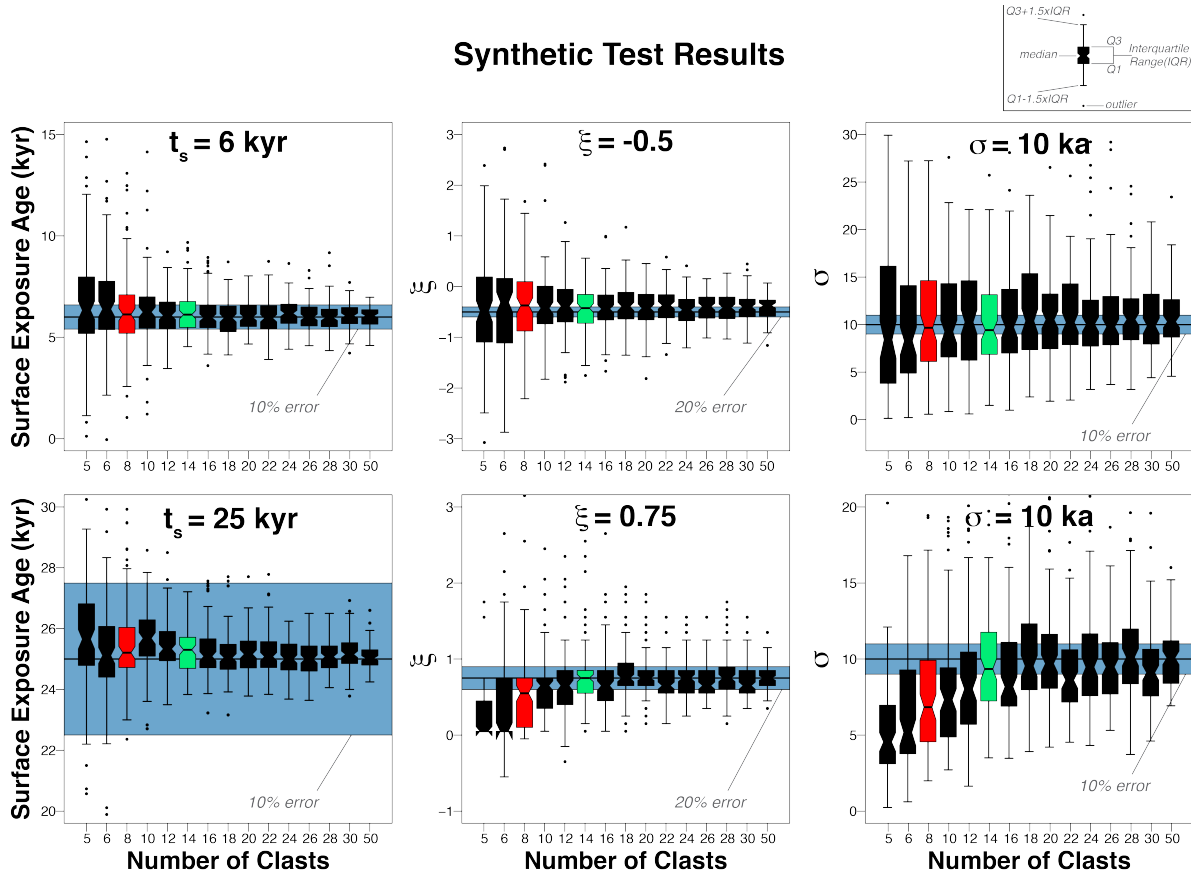
#### 271 **3.1 Synthetic tests**

272 Given the small sample sizes of most available published datasets, the distribution of  
273 clast ages may not be adequately sampled to correctly model the GPD. In order to determine a  
274 viable sample size for fitting the GPD to clast-age distributions, we used our MCMC algorithm  
275 to fit the GPD to synthetically generated GPD datasets (Fig. 4). We sampled from two known  
276 distributions where  $\xi = -0.5$  (upper row, Fig. 4) and  $\xi = 0.75$  (lower row, Fig. 4). For the  
277 known distribution with a negative-valued  $\xi$ , we set  $t_s = 5$  ka. For the positive-valued  $\xi$  dataset,  
278  $t_s = 25$  ka. For both datasets, we set  $\sigma = 10$  ka. For both known distributions, we generated

279 random samples ranging from 5 to 50 individual measurements (equivalent to 5 or 50 cobble or  
280 boulder measurements). For each possible dataset size, we generated 100 random realizations  
281 and produced a model result for each.

282 Our synthetic tests show that the GPD CDF should ideally be fit to 14 or more samples.  
283 Estimates for surface age ( $t_s$ ) and shape ( $\xi$ ) converge more readily than distribution scale ( $\sigma$ ).  
284 At sample sizes greater than 14, decreased uncertainty in GPD parameters is offset by production  
285 rate uncertainty, which we take to be ~10-20% (e.g., Borchers et al., 2016; Lifton et al., 2014;  
286 Marrero et al., 2016; Phillips et al., 2016). Because few published datasets with 14 or more  
287 individual clast measurements exist globally ( $n = 6$ ), we set a lower threshold of 8 individual  
288 clast measurements to balance adequate representation of the GPD while casting more widely  
289 across the published literature ( $n = 64$ ).

290



291

292 **Fig. 4.** Whisker plot results of synthetic tests fitting the GPD model to randomly sampled, known

293 distributions, arranged by increasing sample number. Note that horizontal axis scale is nonlinear.

294 Boxes show the interquartile range for 100 synthetic tests of varying dataset sizes. Explanatory

295 whisker plot output shown at upper right. Blue bands show 10% ( $t_s, \sigma$ ) or 20% ( $\xi$ ) acceptable

296 range for fit distribution parameters. Synthetic tests illustrate the effect of low sample size on

297 model outputs for two representative cases: upper row,  $\xi = -0.5$ ; lower row:  $\xi = 0.75$ .

298 Although  $n = 8$  (red whisker plot) datasets have a higher spread in output parameter values than

299 larger synthetically tested dataset sizes, it is sufficient improvement over  $n = 5$  to justify culling

300 smaller sample sizes. These tests suggest that future studies should strive for datasets of at least  $n$

301  $= 14$  (green whisker plot) to adequately characterize the GPD.

302 **3.2 Application to published data sets**

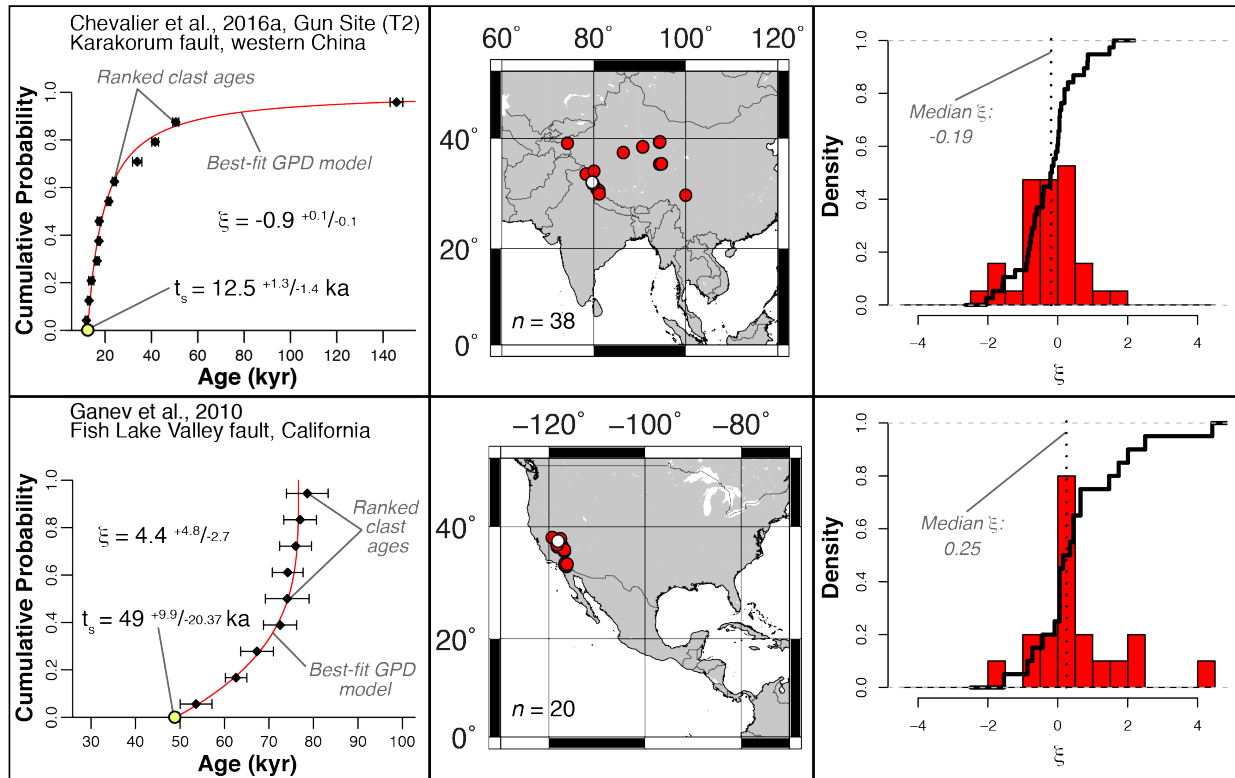


303 To demonstrate the applicability of the GPD clast-age model, we estimate the best-fit  
304 CDF for 64 clast-age distributions from  $^{10}\text{Be}$  datasets drawn from the literature (Fig. 5, Tables S1  
305 and S2, Data S1). All were collected to date stream terraces and alluvial fans, with the majority  
306 displaced by active faults (Table S1). We use the authors' calculated exposure ages at the sample  
307 site and neglect the impact of increasing production rate with catchment elevation (Lal, 1991).  
308 This is valid for determining target surface age, and should not affect estimates of  $\xi$  unless  
309 landslide frequency and background erosion rate vary with elevation or if the grains sampled are  
310 dominantly produced in limited parts of the landscape (Lukens et al., 2016; Riebe et al., 2015).

311 We filter the global datasets to ensure that each dataset represents a single catchment  
312 source, consists only of single clasts, and includes  $\geq 8$  measurements. The majority of data  
313 meeting these criteria come from either southwest North America ( $n = 20$ ) or Asia ( $n = 38$ ),  
314 where exposure age-dating has been widely applied to fault slip-rate studies. Six additional  
315 datasets are found in Peru ( $n = 3$ ) and along the Dead Sea fault zone ( $n = 3$ ). A summary table of  
316 final GPD outputs determined using the MCMC algorithm is presented in Table S2. Over 45% of

317 our GPD model fits (29/64) result in negative  $\xi$  values, with the majority of these collected in  
 318 interior Asia (Fig. 5).

319



320

321 **Fig. 5.** Comparison of typical datasets from the American southwest and Asia. Datasets from the

322 American southwest are more often characterized by  $\xi \geq 0$  (lower panel, Ganev et al., 2010).

323 Datasets from Asia tend towards  $\xi < 0$  (upper panel, Chevalier et al., 2016). Red points show

324 geographic distribution of datasets in these regions. White points indicate locations of example

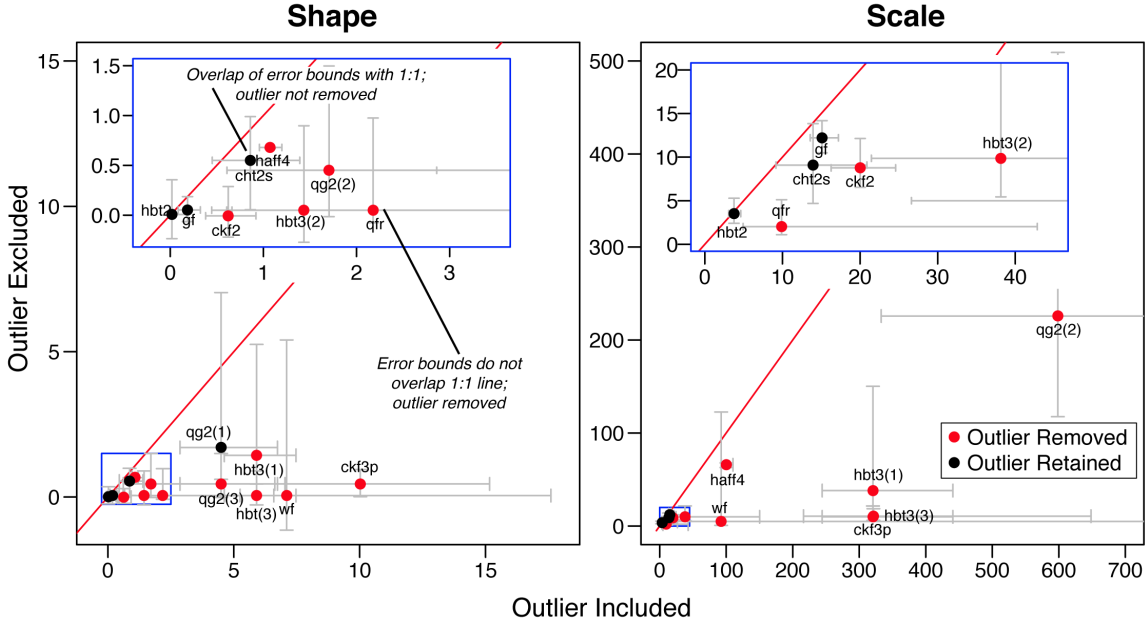
325 datasets at left. Right column shows histograms and empirical CDFs of observed  $\xi$  values in Asia

326 (upper panel) and the American southwest (lower panel).

327

328 **3.3 Identification and removal of young outliers in clast-age distributions**

329 All outliers identified by the publishing authors are included in our models, with the  
330 exception of seven datasets where young outliers cause a statistically significant shift in the  $\xi$   
331 parameter of the best-fit distribution. We interpret these outliers as clasts that either toppled or  
332 were exhumed by erosion of the sampled deposit. We identified by visual inspection ten datasets  
333 from seven publications that contain possible young outliers (Fig. 6, Table S3). To objectively  
334 identify these outliers, we remove samples from datasets based on the statistical significance of  
335 the change to the  $\sigma$  and  $\xi$  parameters they impose on the resultant best-fit GPD distribution. For  
336 all datasets suspected of containing young outliers, we calculate two best-fit GPD distributions:  
337 one that includes the suspected outlier sample, and one where the outliers are removed. If more  
338 than one young outlier is suspected, we calculate as many additional GPD distributions as there  
339 are suspected outliers (Table S3). If the best-fit shape parameter calculated for the dataset  
340 following outlier removal deviates from the 95% confidence range of the  $\xi$  parameter calculated  
341 when the suspected outlier is included, then the outlier is removed (Fig. 6, Fig. S1). We take this  
342 conservative approach to outlier removal in order to restrict the amount of subjective culling of  
343 samples from these datasets. Of the ten datasets that were flagged for containing potential young  
344 outliers, seven were confirmed to include outliers according to our criteria (Table S3).



345  
 346 **Fig. 6.** Methodology of outlier removal for selected datasets. Axes indicate best-fits and 95%  
 347 error bounds to shape ( $\xi$ ) and scale ( $\sigma$ ) parameters for datasets where outlier is included (vertical  
 348 axis) and where outlier is excluded (horizontal axis). Units of  $\xi$  are dimensionless. Units of  $\sigma$  are  
 349 in kyr. Blue boxes in both figures indicate inset region. Outliers are removed if error bounds do  
 350 not cross 1:1 line (red), indicating a statistically significant change in fit of parameters due to  
 351 outlier removal. See Table S3 for label key and parameter outputs for each dataset and removal  
 352 decision. The  $\sigma$  fit to the Qg2 surface (Dühnforth et al., 2017) with no outliers removed plots  
 353 well outside of shown range; comparisons of removal of two outliers are therefore not included  
 354 but are given in Table S3. Only one dataset recorded a statistically significant change in  $\xi$  that  
 355 was not accompanied by a significant change in  $\sigma$  (wf; Zehfuss et al., 2001); we removed the  
 356 outlier from this dataset as well.

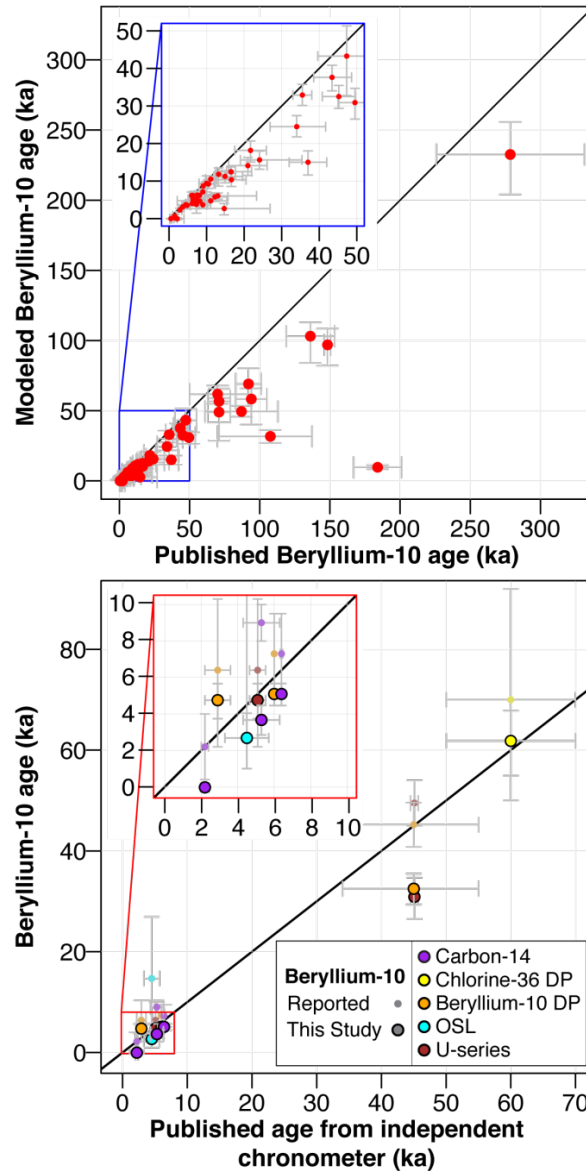
357

358 **4. Discussion**

359 An immediate and widely applicable result of our GPD clast-age model is a rigorous  
360 estimate of the exposure age of a target surface. Using our algorithm, the best-fit  $t_s$  value of the  
361 GPD is the target deposit age, with uncertainty derived from the MCMC analysis (Fig. 3). The  
362 GPD model yields younger surface ages than reported by the publishing authors (Fig. 7a).  
363 Importantly, when  $\xi < 1$ , the clustering of the youngest samples defines a rank-age slope of the  
364 GPD, and therefore estimates of  $t_s$  are not overly sensitive to sampling the youngest available  
365 surface clast (Fig. 3).

366 To validate age estimations from the GPD model, we compare our results with  
367 independent geochronometers used by publishing authors at ten sites (Fig. 7b), including TCN  
368 depth-profiles (Anderson et al., 1996). We find that  $t_s$  agrees with these independent ages, with  
369 the exception of four sites with older Carbon-14 dates from materials collected within the  
370 underlying deposits, as should be expected, and two sites where the fitted location parameter  
371 clearly underestimates U-series ages from soil carbonates and a  $^{10}\text{Be}$  depth profile. In these  
372 cases, erosion of the target surfaces has led to exhumation of clasts from the alluvial fan deposits,  
373 with incomplete exposure over the lifetime of the fan surfaces (Behr et al., 2010; Blisniuk et al.,  
374 2013). Our inheritance model does not account for the effects of post-depositional modification  
375 of target surfaces. Generally, erosion is less of a concern for clasts that are too large to be  
376 transported across stable fan surfaces, unless erosion of surrounding materials has been sufficient

377 to exhume clasts from depth (e.g. Behr et al., 2010). Most of the sites we examine are young  
378 deposits (<50 ka) and unlikely to have eroded sufficiently to expose younger clasts.



379  
380 **Fig. 7.**  $^{10}\text{Be}$  age adjustments and comparison with additional geochronometers. Top: Comparison  
381 between published and modeled ages determined from  $^{10}\text{Be}$  surface clast datasets. Note  
382 systematically younger modeled ages. Bottom: Comparison of published and modeled ages with  
383 independent geochronometers, including TCN depth profiles, as reported by publishing authors.

384 In most cases our modeled ages lie closer to the independent ages, indicated by the 1:1 line.  
385 Annotated version of lower figure included in extended data (Fig. S1).

386

387 Negative  $\xi$  values occur frequently in the arid interior of Asia and a subset of the most  
388 arid regions of the southwestern United States. These populations are characterized by strongly  
389 curved, concave-down cumulative age distributions (Fig. 1), with the oldest clasts several tens of  
390 thousands of years older than the youngest. The commonality of these long-tailed distributions  
391 argues against contamination by recycled sediments as a rationale for removal of older ages as  
392 outliers. We hypothesize that long-tailed populations of clast ages appear in these settings  
393 because of negligible background erosion, such that the underlying distribution of landslide wait  
394 times largely controls the exposure of bedrock. Long-tailed (e.g. Pareto-distributed) landslide  
395 recurrence behavior likely occurs in more humid settings as well, but is obscured by higher rates  
396 of background erosion. With infrequent landslides, clast-age distributions derived with Pareto-  
397 distributed landslide recurrence (eq. 8) become indistinguishable from the results of a Poisson-  
398 based recurrence model (Fig. 2).

399 A long-tailed distribution of landslide recurrence implies that recent landslide sites are  
400 more likely to be reactivated than areas of longer-term stability. This results in spatial and  
401 temporal clustering of landslide triggering, alternating with time-dependent stabilization of the  
402 landscape. To date, few datasets exist to corroborate such a temporal distribution of landslides at  
403 the catchment scale. A power-law distribution of landslide wait times has been suggested for a  
404 50-year record of landslide activity in Italy (Rossi et al., 2010). Power spectral analyses of this  
405 same dataset confirms temporal clustering (Witt et al., 2010). Temporal clustering of landsliding  
406 may be driven by the underlying distribution of triggering events, such as rainfall or earthquakes

407 (e.g., McPhillips et al., 2014; West et al., 2014). Spatial variation of landslide recurrence time  
408 may correspond to the observed variation of catchment hillslope curvature, from creep-  
409 dominated, strongly curved ridge crests to steep, planar landslide-dominated slopes (e.g., Hurst  
410 et al., 2012; Roering et al., 1999).

411 By fitting the full range of clast ages, our modeling approach yields mean inherited  
412 exposure age,  $\bar{t}_c$ , and thus catchment mean erosion rate,  $E = z^*/\bar{t}_c$ , from the parameters of the  
413 GPD distribution. This complements the widely applied technique of measuring  $\bar{t}_c$  from well-  
414 mixed sand samples (Granger, 2006). The mean value of the GPD,  $\bar{t}_c = \sigma/(1 + \xi)$ , exists for  
415  $\xi > -1$ . A mean value also exists for clast ages predicted from Pareto-distributed landslide  
416 recurrence, even for heavy-tailed cases ( $\xi \leq -1$ ), because the distribution truncates at  $t_b$  (Fig.  
417 1).

418 Our mechanistic model for the distribution of clast exposure ages provides a rationale for  
419 removing inheritance from landform ages and a framework for assessing landslide recurrence  
420 behavior and erosion rate from the distribution parameters. By revealing the balance of physical  
421 erosion mechanisms, clast populations can provide essential information for understanding  
422 chemical cycling through the critical zone. Because the distribution of clast ages is insensitive to  
423 post-depositional exposure history, this tool may be applied to ancient deposits as well as  
424 modern river sediments. The frequent occurrence of long-tailed clast-age populations suggests  
425 that landslide wait times are Pareto-distributed, and thus temporally or spatially clustered, with  
426 important implications for quantifying landslide hazard. Reduction in surface age of all datasets



427 examined in this study necessitates a reevaluation of fault slip rates at the original study sites,  
428 which will influence models of earthquake hazard.

429

#### 430 **4. Conclusions**

431 We present a mechanistic model of inheritance recorded in surface clast datasets that  
432 encompasses the effects of episodic landsliding and steady background erosion on recorded TCN  
433 concentration. We propose that a generalized Pareto distribution characterized by three  
434 parameters – post-depositional surface age ( $t_s$ ), shape ( $\xi$ ), and scale ( $\sigma$ ) – should be used to fit  
435 clast-age distributions. For the case of Poisson landslide recurrence, the scale parameter  
436 corresponds to mean landslide recurrence time and the shape parameter is the ratio of  
437 background erosion timescale to this recurrence time. To apply the GPD distribution, we  
438 developed a Monte Carlo Markov Chain algorithm to fit this model to surface clast datasets. By  
439 fitting the GPD to 64 Beryllium-10 datasets drawn from a global literature survey, we show that  
440 this model can be applied to clast-age distributions sourced from a variety of geographic settings.

441 The abundance of datasets with negative  $\xi$  indicates that a Poisson model of landslide  
442 return time is inadequate. We propose a Pareto landslide wait time model to explain these  
443 datasets, and show that this model may be approximated by the GPD where background erosion  
444 rates are low. In other settings, it is difficult to discriminate Poisson- and Pareto-based landslide  
445 recurrence, given the small sample sizes of current Beryllium-10 datasets.

446 Application of our GPD model results in younger surface ages than previously published.  
447 We show that in most cases, our new age determinations better correspond to ages from  
448 independent Quaternary geochronometers. In addition to improved exposure age dating, the  
449 distribution of clast ages reveals the balance of erosion processes operating across the landscape.

450 This opens the door to new applications of TCN geochronology to quantify erosion in upstream  
451 catchments.

452

453

#### 454 **Acknowledgments**

455 The authors thank Lewis Owen and Jing Liu-Zeng for numerous discussions that helped in the  
456 development of this project. We thank Magali Billen, Maxwell Rudolph, Isabel Montañez, Sujoy  
457 Mukhopadhyay, and Don Turcotte for early reviews of the manuscript. This effort was supported  
458 by National Science Foundation [award number EAR-1524734] and the Southern California  
459 Earthquake Center [grants #15209 and #17121].

460

461 Both authors contributed equally to the preparation of this manuscript. The authors declare no  
462 competing interests.

463

#### 464 **References**

465 Anderson, R.S., Repka, J.L., Dick, G.S., 1996. Explicit treatment of inheritance in dating  
466 depositional surfaces using in situ  $^{10}\text{Be}$  and  $^{26}\text{Al}$ . *Geology* 24, 47–51.

467 [https://doi.org/10.1130/0091-7613\(1996\)024<0047:ETOID>2.3.CO](https://doi.org/10.1130/0091-7613(1996)024<0047:ETOID>2.3.CO)

468 Andrieu, C., De Freitas, N., Doucet, A., Jordan, M.I., 2003. An introduction to MCMC for  
469 machine learning. *Mach. Learn.* 50, 5–43. <https://doi.org/10.1023/A:1020281327116>

470 Behr, W.M., Rood, D.H., Fletcher, K.E., Guzman, N., Finkel, R., Hanks, T.C., Hudnut, K.W.,

471 Kendrick, K.J., Platt, J.P., Sharp, W.D., Weldon, R.J., Yule, J.D., 2010. Uncertainties in

472 slip-rate estimates for the Mission Creek strand of the southern San Andreas fault at Biskra

- 473 Palms Oasis, southern California. *Bull. Geol. Soc. Am.* 122, 1360–1377.  
474 <https://doi.org/10.1130/B30020.1>
- 475 Blisniuk, K., Oskin, M., Mériaux, A.S., Rockwell, T., Finkel, R.C., Ryerson, F.J., 2013. Stable,  
476 rapid rate of slip since inception of the San Jacinto fault, California. *Geophys. Res. Lett.* 40,  
477 4209–4213. <https://doi.org/10.1002/grl.50819>
- 478 Borchers, B., Marrero, S., Balco, G., Caffee, M., Goehring, B., Lifton, N., Nishiizumi, K.,  
479 Phillips, F., Schaefer, J., Stone, J., 2016. Geological calibration of spallation production  
480 rates in the CRONUS-Earth project. *Quat. Geochronol.* 31, 188–198.  
481 <https://doi.org/10.1016/j.quageo.2015.01.009>
- 482 Brown, E.T., Stallard, R.F., Larsen, M.C., Raisbeck, G.M., Yiou, F., 1995. Denudation rates  
483 determined from the accumulation of in situ-produced  $^{10}\text{Be}$  in the luquillo experimental  
484 forest, Puerto Rico. *Earth Planet. Sci. Lett.* 129, 193–202. [https://doi.org/10.1016/0012-](https://doi.org/10.1016/0012-821X(94)00249-X)  
485 [821X\(94\)00249-X](https://doi.org/10.1016/0012-821X(94)00249-X)
- 486 Cerling, T.E., Craig, H., 1994. Geomorphology and In-Situ Cosmogenic Isotopes. *Annu. Rev.*  
487 *Earth Planet. Sci.* 22, 273–317.
- 488 Chevalier, M.L., Der Woerd, J. Van, Tapponnier, P., Li, H., Ryerson, F.J., Finkel, R.C., 2016.  
489 Late Quaternary slip-rate along the central Bangong-Chaxikang segment of the Karakorum  
490 fault, western Tibet. *Bull. Geol. Soc. Am.* 128, 284–314. <https://doi.org/10.1130/B31269>
- 491 Crovelli, R.A., 2000. Probability models for estimation of number and costs of landslides, US  
492 Geological Survey Open-File Report 00-249.
- 493 Dadson, S.J., Hovius, N., Chen, H., Dade, W.B., Hsieh, M.-L., Willett, S.D., Hu, J.-C., Horng,  
494 M.-J., Chen, M.-C., Stark, C.P., Lague, D., Lin, J.-C., 2003. Links between erosion, runoff  
495 variability and seismicity in the Taiwan orogen. *Nature* 426, 648–651.

- 496 de Zea Bermudez, P., Kotz, S., 2010. Parameter estimation of the generalized Pareto distribution-  
497 Part I. *J. Stat. Plan. Inference* 140, 1353–1373. <https://doi.org/10.1016/j.jspi.2008.11.020>
- 498 Dühnforth, M., Densmore, A.L., Ivy-Ochs, S., Allen, P., Kubik, P.W., 2017. Early to Late  
499 Pleistocene history of debris-flow fan evolution in western Death Valley (California) using  
500 cosmogenic  $^{10}\text{Be}$  and  $^{26}\text{Al}$ . *Geomorphology* 281, 53–65.  
501 <https://doi.org/10.1016/j.geomorph.2016.12.020>
- 502 Emberson, R., Hovius, N., Galy, A., Marc, O., 2016. Chemical weathering in active mountain  
503 belts controlled by stochastic bedrock landsliding. *Nat. Geosci.* 9, 42–45.  
504 <https://doi.org/10.1038/ngeo2600>
- 505 Gabet, E.J., 2007. A theoretical model coupling chemical weathering and physical erosion in  
506 landslide-dominated landscapes. *Earth Planet. Sci. Lett.* 264, 259–265.  
507 <https://doi.org/10.1016/j.epsl.2007.09.028>
- 508 Ganev, P.N., Dolan, J.F., Frankel, K.L., Finkel, R.C., 2010. Rates of extension along the Fish  
509 Lake Valley fault and transtensional deformation in the Eastern California shear zone-  
510 Walker Lane belt. *Lithosphere* 2, 33–49. <https://doi.org/10.1130/L51.1>
- 511 Gosse, J.C., Phillips, F.M., 2001. Terrestrial in situ cosmogenic nuclides: theory and application.  
512 *Quat. Sci. Rev.* 20, 1475–1560.
- 513 Granger, D.E., 2006. A review of burial dating methods using  $^{26}\text{Al}$  and  $^{10}\text{Be}$  A review of  
514 burial dating methods using  $^{26}\text{Al}$  and  $^{10}\text{Be}$ . *Geol. Soc. Am. Spec. Pap.* 415, 1–16.  
515 [https://doi.org/10.1130/2006.2415\(01\)](https://doi.org/10.1130/2006.2415(01)).
- 516 Granger, D.E., Riebe, C.S., 2013. *Cosmogenic Nuclides in Weathering and Erosion*, 2nd ed,  
517 *Treatise on Geochemistry: Second Edition*. Elsevier Ltd. <https://doi.org/10.1016/B978-0-08-095975-7.00514-3>  
518

- 519 Hosking, J.R.M., Wallis, J.R., 1987. Parameter and quantile estimation for the generalized Pareto  
520 distribution. *Technometrics* 29, 339–349. <https://doi.org/10.2307/1269343>
- 521 Hurst, M.D., Mudd, S.M., Walcott, R., Attal, M., Yoo, K., 2012. Using hilltop curvature to  
522 derive the spatial distribution of erosion rates. *J. Geophys. Res.* 117, F02017.  
523 <https://doi.org/10.1029/2011JF002057>
- 524 Korup, O., Densmore, A.L., Schlunegger, F., 2010. The role of landslides in mountain range  
525 evolution. *Geomorphology* 120, 77–90. <https://doi.org/10.1016/j.geomorph.2009.09.017>
- 526 Kump, L.R., Brantley, S.L., Arthur, M.A., 2000. Chemical Weathering, Atmospheric CO<sub>2</sub>, and  
527 Climate. *Annu. Rev. Earth Planet. Sci.* 28, 611–667.
- 528 Lal, D., 1991. Cosmic ray labeling of erosion surfaces: in situ nuclide production rates and  
529 erosion models. *Earth Planet. Sci. Lett.* 104, 424–439.
- 530 Lifton, N., Sato, T., Dunai, T.J., 2014. Scaling in situ cosmogenic nuclide production rates using  
531 analytical approximations to atmospheric cosmic-ray fluxes. *Earth Planet. Sci. Lett.* 386,  
532 149–160. <https://doi.org/10.1016/j.epsl.2013.10.052>
- 533 Lomax, K.S., 2012. Business Failures : Another Example of the Analysis of Failure Data 1459.
- 534 Lukens, C.E., Riebe, C.S., Sklar, L.S., Shuster, D.L., 2016. Grain size bias in cosmogenic  
535 nuclide studies of stream sediment in steep terrain.  
536 <https://doi.org/10.1002/2016JF003859>.Received
- 537 Marrero, S.M., Phillips, F.M., Borchers, B., Lifton, N., Aumer, R., Balco, G., 2016. Cosmogenic  
538 nuclide systematics and the CRONUScalc program. *Quat. Geochronol.* 31, 160–187.  
539 <https://doi.org/10.1016/j.quageo.2015.09.005>
- 540 McPhillips, D., Bierman, P.R., Rood, D.H., 2014. Millennial-scale record of landslides in the  
541 Andes consistent with earthquake trigger. *Nat. Geosci.* 7, 925–930.

- 542 <https://doi.org/10.1038/ngeo2278>
- 543 Niemi, N.A., Oskin, M., Burbank, D.W., Heimsath, A.M., Gabet, E.J., 2005. Effects of bedrock  
544 landslides on cosmogenically determined erosion rates. *Earth Planet. Sci. Lett.* 237, 480–  
545 498. <https://doi.org/10.1016/j.epsl.2005.07.009>
- 546 Page, M.T., Field, E.H., Milner, K.R., Powers, P.M., 2014. The UCERF3 Grand Inversion :  
547 Solving for the Long-Term Rate of Ruptures in a Fault System. *Bull. Seismol. Soc. Am.*  
548 104, 1181–1204. <https://doi.org/10.1785/0120130180>
- 549 Phillips, F.M., Argento, D.C., Balco, G., Caffee, M.W., Clem, J., Dunai, T.J., Finkel, R.,  
550 Goehring, B., Gosse, J.C., Hudson, A.M., Jull, A.J.T., Kelly, M.A., Kurz, M., Lal, D.,  
551 Lifton, N., Marrero, S.M., Nishiizumi, K., Reedy, R.C., Schaefer, J., Stone, J.O.H.,  
552 Swanson, T., Zreda, M.G., 2016. Quaternary Geochronology The CRONUS-Earth Project :  
553 A synthesis. *Quat. Geochronol.* 31, 119–154. <https://doi.org/10.1016/j.quageo.2015.09.006>
- 554 Riebe, C.S., Sklar, L.S., Lukens, C.E., Shuster, D.L., 2015. Climate and topography control the  
555 size and flux of sediment produced on steep mountain slopes. *Proc. Natl. Acad. Sci.* 112,  
556 201503567. <https://doi.org/10.1073/pnas.1503567112>
- 557 Roering, J.J., Kirchner, J.W., Dietrich, W.E., 1999. Evidence for nonlinear, diffusive sediment  
558 transport on hillslopes and implications for landscape morphology. *Water Resour. Res.* 35,  
559 853–870. <https://doi.org/10.1029/1998WR900090>
- 560 Rossi, M., Witt, A., Guzzetti, F., Malamud, B.D., Peruccacci, S., 2010. Analysis of historical  
561 landslide time series in the Emilia-Romagna region, northern Italy. *Earth Surf. Process.*  
562 *Landforms* 35, 1123–1137. <https://doi.org/10.1002/esp.1858>
- 563 Szalvadori, G., 2002. Linear combinations of order statistics to estimate the position and scale  
564 parameters of the Generalized Pareto distribution. *Stoch. Environ. Res. Risk Assess.* 16.

- 565 <https://doi.org/10.1007/s00477-001-0080-2>
- 566 Stone, J.O., 2000. Air pressure and cosmogenic isotope production. *J. Geophys. Res.* 105,  
567 23753–23759.
- 568 Taylor, A., Blum, J.D., 1995. Relation between soil age and silicate weathering rates determined  
569 from the chemical evolution of a glacial chronosequence. *Geology* 23, 979–982.  
570 [https://doi.org/10.1130/0091-7613\(1995\)023<0979:RBSAAS>2.3.CO](https://doi.org/10.1130/0091-7613(1995)023<0979:RBSAAS>2.3.CO)
- 571 Van Der Woerd, J., Tapponnier, P., Ryerson, F.J., Mériaux, A., Meyer, B., Gaudemer, Y.,  
572 Finkel, R.C., Caffee, M.W., Guoguang, Z., Zhiqin, X., 2002. Uniform postglacial slip-rate  
573 along the central 600 km of the Kunlun Fault (Tibet), from <sup>26</sup>Al, <sup>10</sup>Be, and <sup>14</sup>C dating of  
574 riser offsets, and climatic origin of the regional morphology. *Geophys. J. Int.* 356–388.
- 575 West, A.J., Hetzel, R., Li, G., Jin, Z., Zhang, F., Hilton, R.G., Densmore, A.L., 2014. Dilution of  
576 <sup>10</sup>Be in detrital quartz by earthquake-induced landslides: Implications for determining  
577 denudation rates and potential to provide insights into landslide sediment dynamics. *Earth  
578 Planet. Sci. Lett.* 396, 143–153. <https://doi.org/10.1016/j.epsl.2014.03.058>
- 579 Witt, A., Malamud, B.D., Rossi, M., Guzzetti, F., Peruccacci, S., 2010. Temporal correlations  
580 and clustering of landslides. *Earth Surf. Process. Landforms* 35, 1138–1156.  
581 <https://doi.org/10.1002/esp.1998>
- 582 Yanites, B.J., Tucker, G.E., Anderson, R.S., 2009. Numerical and analytical models of  
583 cosmogenic radionuclide dynamics in landslide-dominated drainage basins. *J. Geophys.  
584 Res. Earth Surf.* 114. <https://doi.org/10.1029/2008JF001088>
- 585 Zehfuss, P.H., Bierman, P.R., Gillespie, a. R., Burke, R.M., Caffee, M.W., 2001. Slip rates on  
586 the Fish Springs fault, Owens Valley, California, deduced from cosmogenic <sup>10</sup>Be and <sup>26</sup>Al  
587 and soil development on fan surfaces. *Bull. Geol. Soc. Am.* 113, 241–255.

588 [https://doi.org/10.1130/0016-7606\(2001\)113<0241:SROTFS>2.0.CO;2](https://doi.org/10.1130/0016-7606(2001)113<0241:SROTFS>2.0.CO;2)

589